Article

Not peer-reviewed version

Microstructural and Mechanical Properties of Y_2O_3 Modified Ti6Al4V Alloy Fabricated by Laser Powder Bed Fusion

Jinyu Zhu , Yangping Dong * , Huihua Zhang , Shuming Zhao , Guonan Ma * , Wentian Zhao , Renyi Lu , Pengwei Yang , Guang Yang , Xin Zhang , Yifei Li , Dongzi Wu , Liang Zhong , Peng Xu

Posted Date: 30 January 2026

doi: 10.20944/preprints202601.2384.v1

Keywords: Ti6Al4V;Laser powder bed fusion;Y_2O_3;Additive manufacturing;Microstructure;Mechanical properties

 doi:10.20944/preprints202601.2384.v1

Article

Microstructural and Mechanical Properties of Y_2O_3 Modified Ti6Al4V Alloy Fabricated by Laser Powder Bed Fusion

Jinyu Zhu [1], Yangping Dong [1,*], Huihua Zhang [1], Shuming Zhao [1], Guonan Ma [1,*], Wentian Zhao [1], Renyi Lu [1], Pengwei Yang [1], Guang Yang [1], Xin Zhang [1], Yifei Li [1], Dongzi Wu [1], Liang Zhong [1] and Peng Xu [2]

[1] Ningbo Branch of Chinese Academy of Ordnance Science, Ningbo, 315103, China

[2] Department of Materials Science and Engineering, Southern University of Science and Technology, Shenzhen 518055, China

* Correspondence: dyp0802@126.com (Y.D.); Ma_Guonan@163.com (G.M.)

Abstract

A Ti6Al4V alloy fabrication via laser powder bed fusion (L-PBF) leads to the formation of coarse columnar β grains that give rise to anisotropic mechanical properties and inadequate strength. Incorporating the rare earth oxide, yttrium oxide (Y_2O_3), has proven an effective strategy in enhancing the mechanical performance of Ti6Al4V alloys. This study systematically investigates the effects of various Y_2O_3 contents on the microstructure and mechanical properties of Ti6Al4V alloys fabricated via L-PBF. The results demonstrate that a Y_2O_3 addition of 0.2 wt.% produces β grains and α phases with average sizes of 61.6 and 7.6 μm, respectively. Transmission electron microscopy observations reveal that Y_2O_3 nanoparticles, together with elemental Y nanoparticles formed by reduction, are distributed both within the α-Ti matrix and along phase boundaries. This distribution effectively reinforces grain boundaries and promotes heterogeneous nucleation, thereby refining the microstructure. Mechanical property tests indicate that the alloy strength significantly improves as the Y_2O_3 content increases. Specifically, the alloy with 0.2 wt.%Y_2O_3 exhibits a tensile strength of 1106 MPa, a yield strength of 1074 MPa, and an elongation of 10.0%. This study proposes an innovative rare earth strengthening method for refining the microstructure of L-PBF-fabricated titanium alloys and comprehensively enhancing their mechanical properties.

Keywords: Ti6Al4V; Laser powder bed fusion; Y_2O_3; Additive manufacturing; Microstructure; Mechanical properties

1. Introduction

Laser powder bed fusion (L-PBF)—a prominent additive manufacturing technology—has been widely adopted owing to its favorable characteristics, including relatively low post-processing surface roughness, high dimensional accuracy of fabricated components, and integrated structural formation. The core principle underpinning L-PBF involves slicing a digital model of the part into layers by system software. Based on the slice data of each layer, a high-energy laser beam then selectively melts the powder. The molten layers are successively accumulated until the final part is fully constructed [1–3].

Titanium and its alloys represent a class of lightweight structural materials characterized by a density of merely 4.45 g/cm³. Among them, Ti6Al4V is an α+β titanium alloy known for its outstanding properties, including high-temperature resistance, corrosion resistance, superior thermal strength, and excellent hot workability. Consequently, Ti6Al4V has achieved extensive application in the defense, biomedical, petrochemical, aerospace, and marine engineering sectors [4–7].

 doi:10.20944/preprints202601.2384.v1

Despite the advantages of L-PBF, its high thermal gradients, extremely rapid solidification rates, and complex thermal history [8–10] produce titanium alloys with a microstructure that predominantly comprises acicular martensite and coarse columnar grains. These microstructural characteristics negatively impact the final mechanical properties of the alloys, rendering them unable to meet engineering application requirements [11–14]. Numerous studies have demonstrated that the addition of rare earth elements is an effective approach for refining the microstructure and enhancing the mechanical properties of titanium alloys [15–18]. Li et al. [19] innovatively incorporated in situ La_2O_3 nanoparticles and TiB nanofibers into composite powders to form an ultrafine network that markedly refined the grain structure. Compared with the original alloy, tensile strength achieved 1098 MPa and elongation increased from 2.2% to 10.8%. Liu et al. [20] introduced trace amounts of yttrium oxide (Y_2O_3) nanoparticles into Ti-4Al-4V (Ti44) alloy powder and processed the material via L-PBF. Y_2O_3 addition was found to refine the α-martensite laths, thereby improving the strength–ductility balance. Zhou et al. [21] studied the effect of La_2O_3 addition on the wear resistance of a Ti-15Mo alloy fabricated via L-PBF. The results indicated that La_2O_3 addition produced significant grain refinement and inhibited grain growth in the L-PBF-processed titanium matrix composite. Consequently, the wear resistance of the composite was enhanced to more than five times that of the Ti-15Mo alloy.

This study employs L-PBF to fabricate a Ti6Al4V alloy, incorporating trace amounts of the rare earth oxide Y_2O_3 (0.1–0.3 wt.%) through planetary ball milling to achieve a homogeneous dispersion of the Y_2O_3 particles. The systematic investigation examines the effect of Y_2O_3 content on the microstructural evolution and mechanical properties of the alloy for improved functional applicability of the L-PBF-processed Ti6Al4V alloy under extreme service conditions.

2. Materials and Methods

2.1. Materials

This study utilized gas-atomized spherical Ti6Al4V alloy powder with a particle size range of 15–53 μm and Hall flow rate of 37.31 s per 50 g, thus satisfying the process requirements of L-PBF. Y_2O_3 powder (99.99% purity) was synthesized via a chemical route. The Ti6Al4V powder was blended with 0.1–0.3 wt.% Y_2O_3 by planetary ball milling for 1 h, with the rotation direction reversed every 30 min. Mixing was performed in 500 g batches, and a total of 7 kg of powder was prepared to fulfill the spreading requirements. Scanning electron microscopy (SEM) analysis confirmed that the Y_2O_3 particles were uniformly dispersed on the surface of the base powder without altering its original spherical morphology (Figure 1).

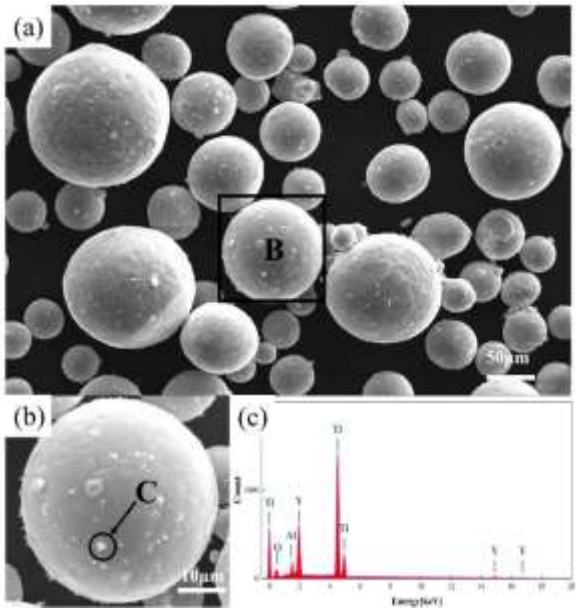

 doi:10.20944/preprints202601.2384.v1

Figure 1. (a) and (b) Morphology of Ti6Al4V-0.3 wt.%Y_2O_3 powder. (c) Energy-dispersive X-ray spectroscopy analysis of the selected region on the powder surface.

2.2. Experimental Method

Specimens were fabricated based on an EOS M290 system using four powder variants—Ti6Al4V, Ti6Al4V-0.1 wt.%Y_2O_3, Ti6Al4V-0.2 wt.%Y_2O_3, and Ti6Al4V-0.3 wt.%Y_2O_3. The processing parameters were set to a layer thickness of 60 μm, laser power of 340 W, hatch spacing of 120 μm, scan speed of 1250 mm/s, substrate preheating temperature of 50 °C, and linear energy density of 37.78 J/mm.

2.3. Microstructural Characterization

The as-printed L-PBF specimens were fabricated as a 1 mm^3 cube to facilitate subsequent microstructural characterization. The as-built specimens were subject to solution and aging heat treatments. Phase identification of the specimens was performed via X-ray diffraction (XRD; Bruker D8). According to the metallographic preparation procedure, the specimens were etched using Kroll's reagent (3% HF + 6% HNO_3 + 91% H_2O), and the effect of different yttria contents on the microstructure was observed via SEM (Gemini SEM 360). The ground and polished specimens underwent further argon ion beam polishing, and their texture orientation and grain size were analyzed via electron backscatter diffraction (EBSD; Gemini SEM 360). The as-printed specimens were wire-cut into thin sheets less than 1 mm thick, and subsequently further thinned by argon ion milling. Phase identification and crystal structure analysis were conducted on the thin sheets via transmission electron microscopy (TEM; JEM-F200).

2.4. Mechanical Properties

This study employed L-PBF to fabricate cylindrical Ti6Al4V alloy specimens, aiming to evaluate the influence of Y_2O_3 on the mechanical properties of the alloy. The specimens were machined into standard tensile specimens with gauge lengths of 25 mm. Tensile testing was performed at room temperature (25 °C) using a universal testing machine (CMT4504) at a constant displacement rate of 1 mm/min. A uniaxial tensile load was applied continuously until fracture, and the corresponding stress–strain curves were recorded. The fracture surfaces of the tested specimens were subsequently examined via SEM to determine their fracture behaviors.

3. Results

3.1. Microstructure and Phase Analysis

Figure 2 presents the XRD patterns of Ti6Al4V-$x$$Y_2O_3$ composites prepared via L-PBF. The phase analysis indicates that the material mainly comprises α-Ti, with a minor amount of β-Ti. Owing to the low concentration of Y_2O_3 and its likely dispersion at the nanoscale, no distinct Y_2O_3 diffraction peaks are detected in the XRD patterns. The detection limit of XRD for minor phases typically ranges from 1% to 5%, and its sensitivity is affected by factors such as the crystallinity, distribution, and mass absorption coefficient of the phase. Therefore, high-resolution SEM and TEM (HRTEM) were deemed necessary to further analyze the morphology, distribution, and interfacial structure of the Y_2O_3 particles within the matrix.

Figure 3 shows the microstructure of the Ti6Al4V-$x$$Y_2O_3$ specimens. In the absence of Y_2O_3 addition, the Ti6Al4V alloy matrix exhibits a dual-phase (α + β) structure. The fine acicular α' martensite observed in the as-deposited condition is fully decomposed, giving rise to lamellar α and small blocky β phases, ultimately forming a characteristic basketweave morphology. With the addition of 0.1 wt.% Y_2O_3, the microstructure exhibits significant changes—the width of the lamellar α phase decreases noticeably, while the area fraction of the gray (α + β) phase regions increase. As the Y_2O_3 content increases further to 0.2 wt.% (Figure 3c, g), the aforementioned trend intensifies—

 doi:10.20944/preprints202601.2384.v1

the lamellar α phase becomes more refined, and the proportion of the grayish-white (α + β) phase increases significantly, nearly dominating the microstructure. However, when the Y_2O_3 content increases to 0.3 wt.%, the microstructural evolution trend reverses—the width of the lamellar α phase increases, and the area fraction of the gray (α + β) phase regions decrease.

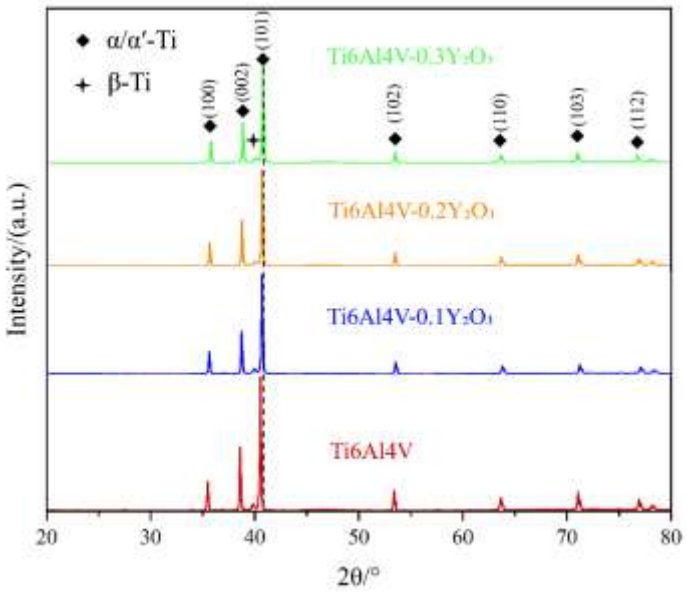

Figure 2. XRD patterns of Ti6Al4V-$x$$Y_2O_3$ alloys.

This microstructural evolution is governed by two principal mechanisms. First, nano-sized Y_2O_3 particles contribute to dispersion strengthening and grain boundary pinning. These particles are uniformly dispersed in the matrix, effectively inhibiting the growth and coarsening of α-phase lamellae and enhancing microstructural refinement [22–24]. Second, yttrium exerts a β-stabilizing influence. At elevated temperatures, the partial decomposition of Y_2O_3 releases Y atoms into solid solution, where they act as β-stabilizing elements. This significantly reduces the $\alpha \rightarrow \beta$ phase transformation temperature, thereby suppressing the transformation of the β phase upon cooling and enabling the retention of a greater amount of high-temperature β phase at room temperature. Consequently, the number and area of the (α + β) phase regions are substantially increased [25].

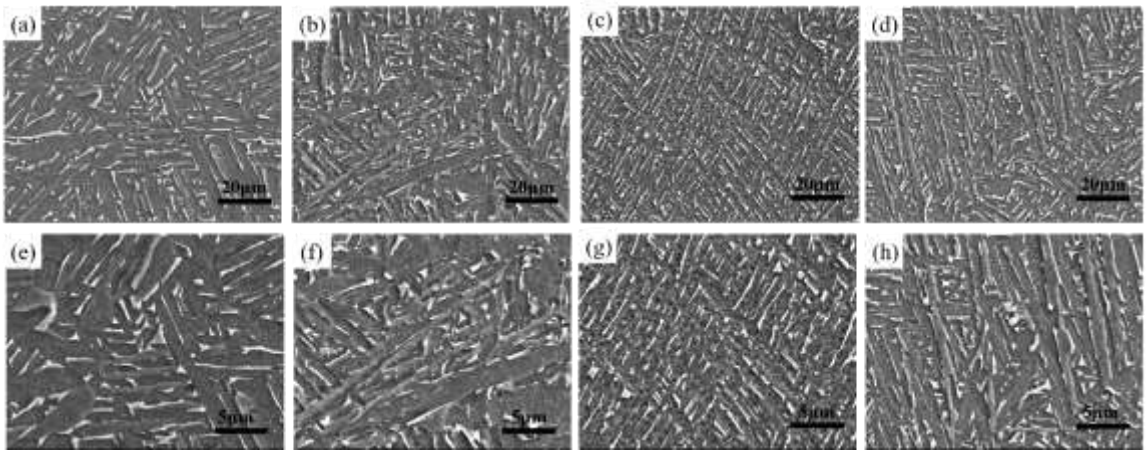

Figure 3. SEM images in the XOY plane of Ti6Al4V-$x$$Y_2O_3$ alloys: (a, e) Ti6Al4V; (b, f) Ti6Al4V with 0.1 wt.%Y_2O_3; (c, g) Ti6Al4V with 0.2 wt.%Y_2O_3; and (d, h) Ti6Al4V with 0.3 wt.%Y_2O_3.

 doi:10.20944/preprints202601.2384.v1

To investigate Ti6Al4V-$x$$Y_2O_3$ alloys, this study used EBSD to analyze the grain morphology, texture orientation, and grain size distribution of four alloys with different Y_2O_3 contents. As shown in Figure 4(a1), the Ti6Al4V alloy without Y_2O_3 addition is predominantly composed of the α-phase with a hexagonal close-packed (HCP) structure—representing approximately 94.6% of the material. A minor fraction of the body-centered cubic (BCC) β-phase—approximately 2.7%—precipitates within the lamellar structure.

From a microstructural standpoint, the alloy exhibits a typical "checkerboard" pattern characterized by uniform coloration within each region. This suggests that α-lath colonies originating from the same prior β grain maintain a consistent crystallographic orientation, whereas noticeable orientation differences arise between lath colonies derived from different prior β grains. To further examine the effect of Y_2O_3 addition on the morphology and evolution of prior β grains in the Ti6Al4V alloy, parent β grains were reconstructed using the classical Burgers orientation relationship for titanium alloys—{110}β//(0001)α and <111>β//<11−20>α—based on the acquired EBSD data [26]. The reconstruction process yielded a more regular β-grain morphology, thereby enabling a more precise analysis of the effect of Y_2O_3 addition on the size, shape, and spatial distribution of β grains.

As shown in Figure 4, Y_2O_3 addition induces a decrease in the β grain size of the alloy relative to the Y_2O_3-free specimen. With the addition of 0.1% Y_2O_3, the average β grain size decreases from 114.3 to 98.2 μm. Upon increasing the Y_2O_3 content to 0.2%, the β grains are further refined to an average size of 61.6 μm. However, when the Y_2O_3 content is increased to 0.3%, the β grain size increases slightly to 71.3 μm. Moreover, Figure 4(c2, d2) shows that the microstructure of the alloy no longer exhibits a typical regular checkerboard pattern, and irregular new grains emerge within certain β grains. This behavior is primarily ascribed to Y_2O_3 particles serving as heterogeneous nucleation sites, which effectively lower the nucleation energy barrier and enhance the nucleation rate, thus facilitating grain refinement. Nevertheless, excessive Y_2O_3 addition may result in the agglomeration of second-phase particles or the formation of a liquid phase, potentially leading to abnormal grain growth.

Figure 5(a) shows the {0001} basal plane pole figure (PF) of hexagonal titanium. A high-intensity region concentrated near the normal direction of the specimen can be observed, with a texture strength of 4.71. As the Y_2O_3 content increases, texture strength significantly decreases. When the Y_2O_3 content reaches 0.2 wt.%, texture strength drops to 2.52. The sequence of PFs in Figure 5(a, b, c) shows that as the Y_2O_3 content increases from 0 wt.% to 0.2 wt.%, the high-value regions (red) gradually weaken, and the overall color distribution shifts toward blue and green tones, indicating a more diffuse grain orientation distribution and significantly reduced degree of preferred orientation [27–29]. When the Y_2O_3 content is further increased to 0.3 wt.%, the texture strength exhibits a slight recovery (Figure 5d).

Figure 6 shows magnified EBSD images of the Ti6Al4V alloy. The left image depicts the microstructure without Y_2O_3 addition, whereas the right image shows the microstructure after the addition of 0.2 wt.% Y_2O_3. The analysis focused on the α-martensite morphology and grain refinement effect, followed by a statistical evaluation of grain size. As shown in Figure 6b–d, compared with the Y_2O_3-free Ti6Al4V alloy (Figure 6a), the addition of different Y_2O_3 contents led to considerable grain refinement. The grain size distribution statistics for the Ti6Al4V and Ti6Al4V–0.2 wt.%Y_2O_3 alloys (Figure 6a–d) reveal a weighted average grain size of 8.4 μm for the Y_2O_3-free Ti6Al4V alloy. In contrast, after the addition of 0.2 wt.%Y_2O_3, the weighted average grain size decreases to 7.6 μm, and the grain texture becomes more random and disordered.

To examine the influence of Y_2O_3 addition on the microstructural evolution of the Ti6Al4V alloy, inverse pole figures (IPFs) corresponding to the (0001), $(\bar{1}2\bar{1}0)$, and $(0\bar{1}10)$ orientations of the α-Ti phase were obtained for both Y_2O_3-free Ti6Al4V and Ti6Al4V with 0.2 wt.% Y_2O_3, as shown in Figure 7. The results reveal that with increasing Y_2O_3 content, the area of the red regions in the IPFs—indicative of strong texture—reduces markedly. This observation reflects a progressive weakening of texture intensity in the α-Ti phase, accompanied by a quantitative decrease in texture strength from 3.35 to 2.46.

 doi:10.20944/preprints202601.2384.v1

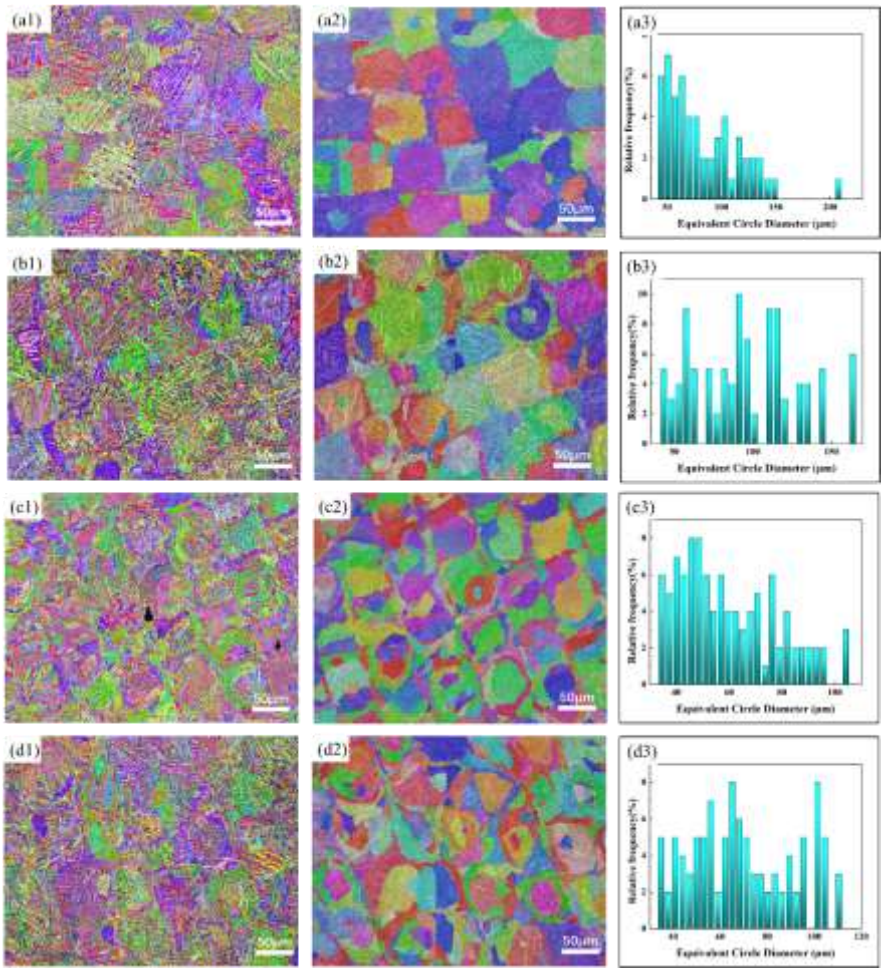

Figure 4. IPF maps of (a1, a2) Ti6Al4V, (b1, b2) Ti6Al4V-0.1 wt.%Y_2O_3, (c1, c2) Ti6Al4V-0.2 wt.%Y_2O_3, and (d1, d2) Ti6Al4V-0.3 wt.%Y_2O_3, along with the corresponding grain size distributions for (a3) Ti6Al4V, (b3) Ti6Al4V-0.1 wt.%Y_2O_3, (c3) Ti6Al4V-0.2 wt.% Y_2O_3, and (d3) Ti6Al4V-0.3 wt.%Y_2O_3.

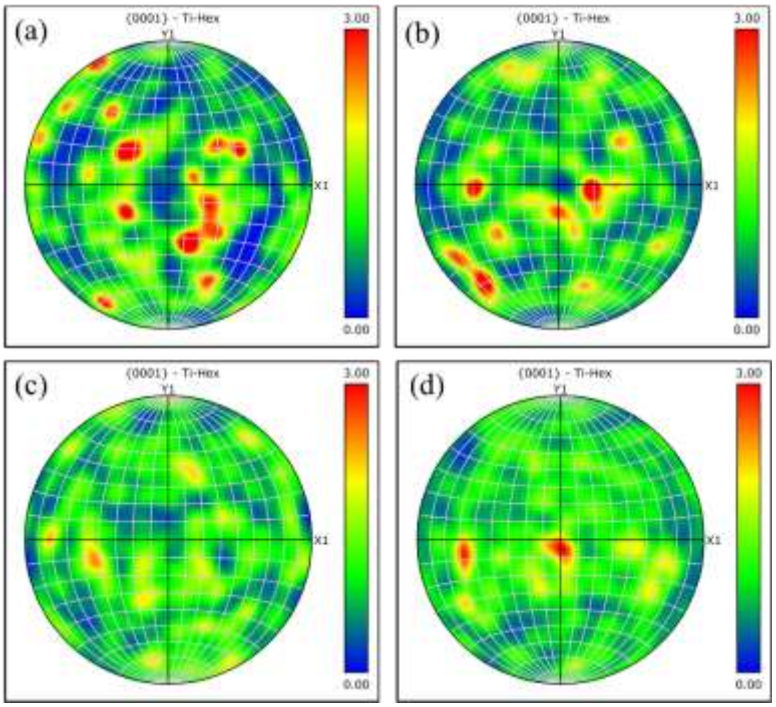

 doi:10.20944/preprints202601.2384.v1

Figure 5. PF maps of (a) Ti6Al4V, (b) Ti6Al4V-0.1 wt.%Y_2O_3, (c) Ti6Al4V-0.2 wt.%Y_2O_3, and (d) Ti6Al4V-0.3 wt.%Y_2O_3.

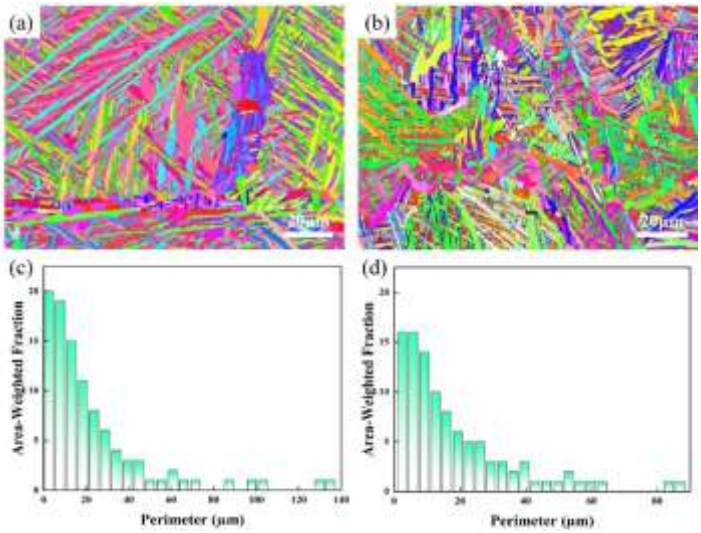

Figure 6. High-magnification EBSD images of Ti6Al4V-$x$$Y_2O_3$ alloys: (a) Ti6Al4V and (b) Ti6Al4V-0.2 wt.%Y_2O_3. (c, d) Grain size distribution of Ti6Al4V and Ti6Al4V-0.2 wt.% Y_2O_3.

Particles tend to accumulate along the grain boundaries or phase boundaries. On one hand, the particles serve as heterogeneous nucleation sites, increasing the nucleation rate and encouraging the transformation of α-phase grains into an equiaxed morphology. However, the particles exert a pinning effect on the grain boundaries, thereby suppressing grain growth during thermal processing. This grain refinement disrupts the initial preferential orientation of the α-Ti phase grains, leading to a reduction in texture intensity. A weaker texture indicates a more random distribution of grain orientations, which in turn reduces the directional dependence of the mechanical properties, thus mitigating anisotropy. In general, reduced anisotropy improves a material's ability to deform uniformly under varying loading directions, thereby enhancing overall mechanical performance—for example, by enabling a better balance between strength and ductility [30].

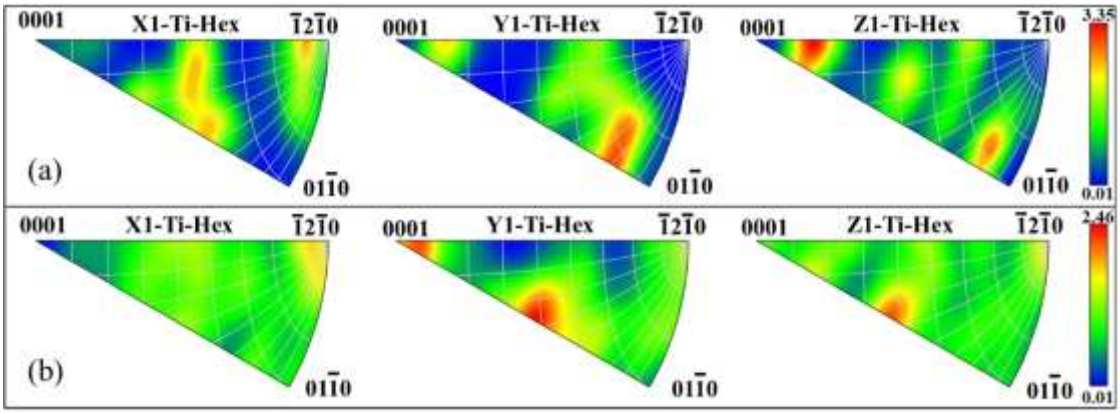

Figure 7. IPFs of the Ti6Al4V-$x$$Y_2O_3$ alloys: (a) Ti6Al4V and (b) Ti6Al4V-0.2 wt.% Y_2O_3.

Figure 8 shows the bright- and dark-field images as well as the corresponding selected area electron diffraction (SAED) pattern of a thin-film specimen obtained from the XOY plane of the central region of the Ti6Al4V-0.2 wt.%Y_2O_3 alloy via ion thinning. The results indicate that the microstructure of the alloy is predominantly composed of lath martensite. The high density of dislocations observed within the α-martensite can supply the necessary energy conditions for

 doi:10.20944/preprints202601.2384.v1

martensite nucleation and growth [31,32]. According to Yang et al. [33], during the L-PBF processing of Ti6Al4V alloys, dislocations can act as favorable sites for martensite nucleation and facilitate the development of martensitic structures, thereby modulating the martensitic transformation process. The incorporated Y_2O_3 particles serve as heterogeneous nucleation sites, indirectly affecting the effective nucleation density of martensite by altering the dislocation density. These findings provide direct insight into the mechanism by which rare earth compounds influence martensite nucleation and its associated size effects.

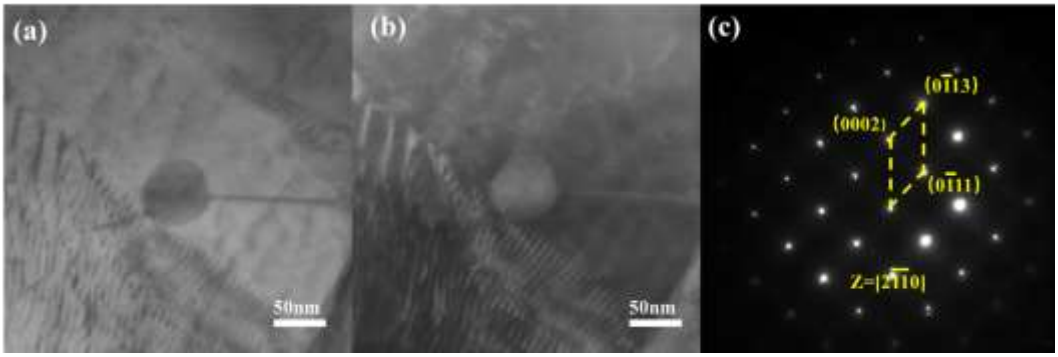

Figure 8. TEM analysis of the Ti6Al4V-0.2 wt.% Y_2O_3 alloy: (a) bright-field image, (b) dark-field image, and (c) selected area electron diffraction pattern.

To elucidate the existence form of the Y element within the α-martensite matrix, the nanoparticles present in the matrix were analyzed via HRTEM. This analysis aimed to ascertain whether the particles comprised discrete Y_2O_3 particles, elemental Y particles, or a combination of both. Figure 9a shows an HRTEM image of a representative nanoparticle, revealing the distinct lattice fringes and crystallographic features. Coupled with the energy-dispersive X-ray spectroscopy (EDS) mapping results—which demonstrated significant enrichment of O and Y in the sampled region—the nanoparticles were preliminarily inferred to be Y_2O_3. Furthermore, the SAED pattern and its corresponding calibration and analysis confirmed the phase identification of the particles.

The α-Ti matrix possessed an HCP crystal structure, with lattice parameters of a = 0.295 nm and c = 0.468 nm. In comparison, Y_2O_3 had a BCC structure with a lattice constant of a = 1.060 nm. Measurements of the interplanar spacings indicated that the characteristic spacing of Y_2O_3 was approximately 0.306 nm, which is consistent with standard crystallographic references for Y_2O_3 and clearly distinct from that of the α-Ti matrix (approximately 0.19 nm) [34]. Indexing of the SAED pattern further confirmed that the Y- and O-enriched nanoparticles correspond to the Y_2O_3 phase.

Another type of nanoparticle was also detected in other regions of the matrix. EDS analysis reveals significant enrichment of Y but no distinct signal of O, preliminarily ruling out the possibility of these particles being Y_2O_3 [35], as shown in Figure 10. SAED analysis of these particles indicated that their diffraction pattern matched the crystal structure of Y element, which has an HCP structure. The typical lattice parameters for Y were a = 0.320 nm and c = 0.514 nm. The measured interplanar spacing of the characteristic crystal planes of Y was approximately 0.325 nm, which is consistent with the crystal structure of Y. Through comparative analysis, we confirmed that the oxygen-free nanoparticles were elemental Y particles. In summary, HRTEM combined with SAED and EDS analyses demonstrated that the nanoscale particles in the α-martensite matrix exist in two forms—Y_2O_3 particles and Y elemental particles.

 doi:10.20944/preprints202601.2384.v1

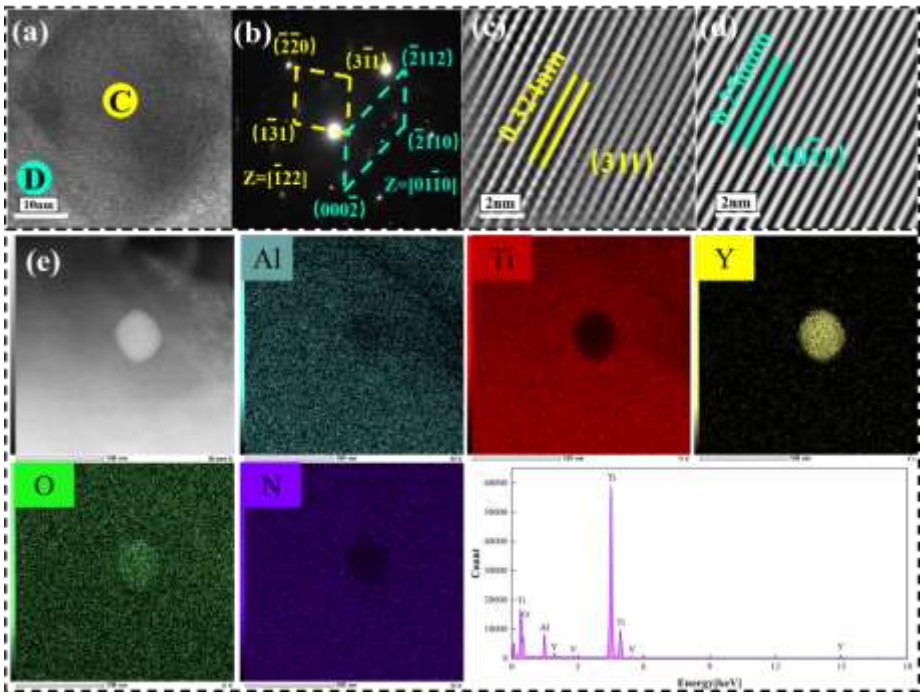

Figure 9. TEM images of Ti6Al4V-0.2 wt.% Y_2O_3: (a) HRTEM image of Y_2O_3/α-Ti, (b) SAED pattern, (c) interplanar spacing map of region "C", (d) interplanar spacing map of region "D", and (e) EDS mapping results for the Y_2O_3 particle.

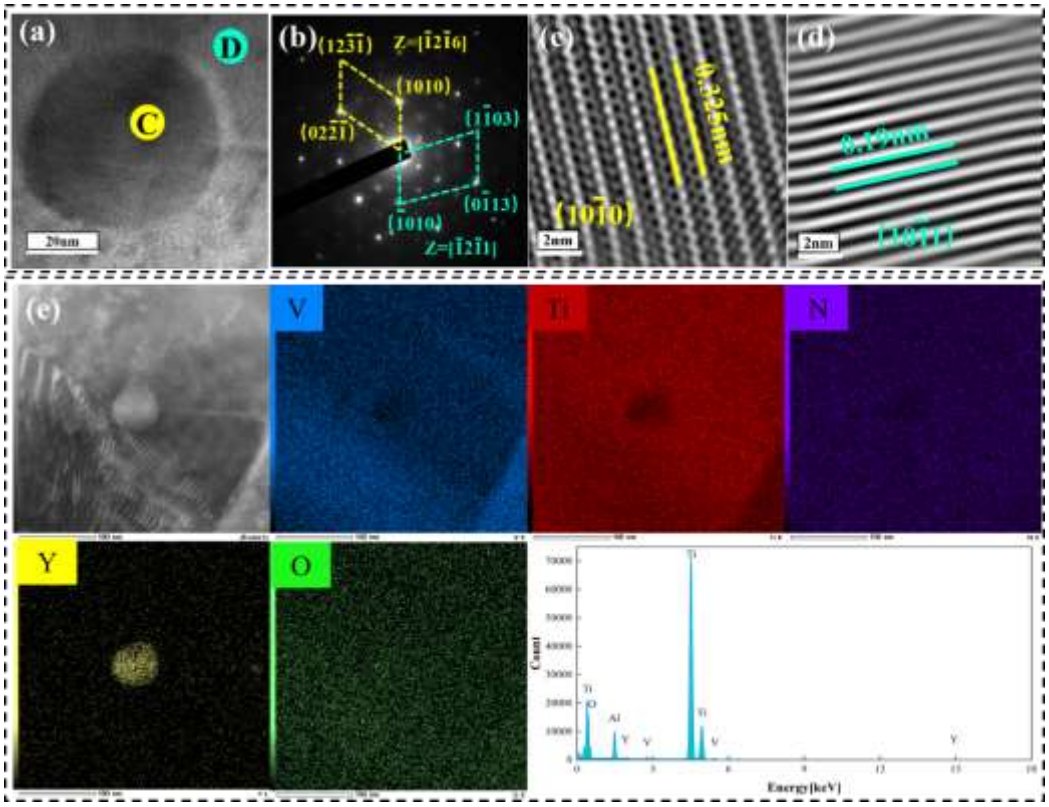

Figure 10. TEM images of Ti6Al4V-0.2 wt.%Y_2O_3: (a) HRTEM image of Y/α-Ti, (b) SAED pattern, (c) interplanar spacing map of region "C", (d) interplanar spacing map of region "D", and (e) EDS mapping results for the Y particle.

 doi:10.20944/preprints202601.2384.v1

3.2. Mechanical properties of the Ti6Al4V-xY_2O_3 alloys

Figure 11 presents the stress-strain curves of tensile specimens prepared along the horizontal direction for L-PBF-fabricated Ti6Al4V-xY_2O_3 composites, with the corresponding mechanical properties summarized in Figure 11. Compared to the Ti6Al4V alloy without Y_2O_3 addition (ultimate tensile strength = 1056 MPa, yield strength = 1001 MPa), the composite with 0.2 wt.% Y_2O_3 exhibits optimal strength performance, with ultimate tensile and yield strengths achieving 1106 and 1074 MPa, respectively, representing increments of 4.7% and 7.3%.

This strength improvement is primarily attributed to the synergistic action of two key micro-mechanisms. First, the added yttrium partially dissolves in the Ti6Al4V matrix, leading to solid solution strengthening. Second, uniformly dispersed nano-sized Y_2O_3 particles within the matrix pin grain boundaries, thereby suppressing grain growth and refining the microstructure while also providing notable dispersion strengthening as second-phase particles. Collectively, these effects enhance both the tensile and yield strengths of the alloy.

However, as strength improves, the ductility of the material tends to decrease with Y_2O_3 addition, as evidenced by the reduction in elongation from 15.4% to 10.0%. This suggests that although Y_2O_3 strengthens the Ti6Al4V alloy, it adversely affects its plasticity. Embrittlement originates primarily from two mechanisms. First, during the high-temperature L-PBF process, partial decomposition of Y_2O_3 releases elemental Y and O, which may elevate the overall O content in the matrix and thereby reduce ductility. Second, Y_2O_3 particles—as a hard ceramic phase—tend to segregate at grain boundaries under rapid solidification. These particles strongly hinder dislocation motion during deformation, producing a pronounced Orowan strengthening effect. Despite the advantages in terms of strength, this mechanism contributes to reduced ductility.

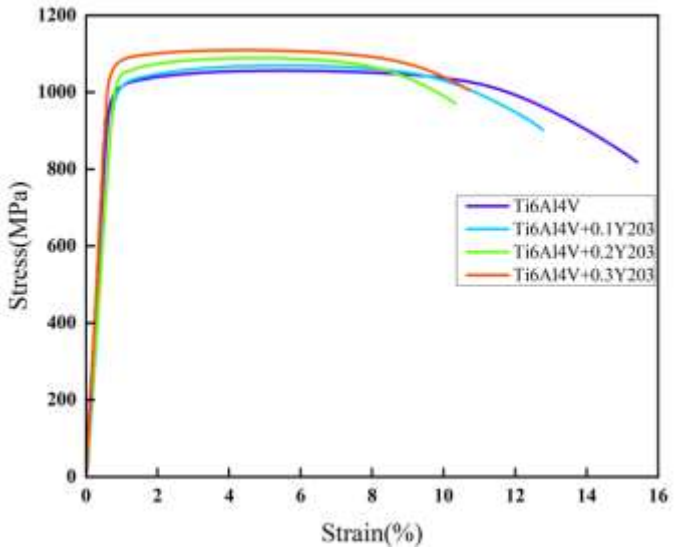

Figure 11. Tensile stress–strain curves of Ti6Al4V-xY_2O_3 alloys.

Figure 12 shows the SEM micrographs of the fracture surfaces of the Ti6Al4V-xY_2O_3 alloys with various Y_2O_3 additions used to systematically examine the effect of Y_2O_3 content on the fracture behavior of the material. Fractographic observations indicate that as the Y_2O_3 content increases, the fracture mechanism of the alloy transitions progressively from ductile to brittle. In particular, the fracture surface of the Y_2O_3-free Ti6Al4V alloy shows typical ductile features, characterized by numerous small, deep equiaxed dimples. With the addition of 0.1% Y_2O_3, the dimple morphology changes markedly—the dimples grow larger and shallower, with reduced uniformity—despite the continued overall ductility of the fracture mode. At 0.2 wt.% Y_2O_3, the fracture morphology exhibits a clear transition—the dimples diminish and quasi-cleavage facets emerge, signaling a shift from

 doi:10.20944/preprints202601.2384.v1

ductile-dominated to quasi-cleavage fracture. At a Y_2O_3 content of 0.3 wt.%, distinct cleavage steps and river patterns are evident on the fracture surface, indicating a predominantly brittle fracture mechanism.

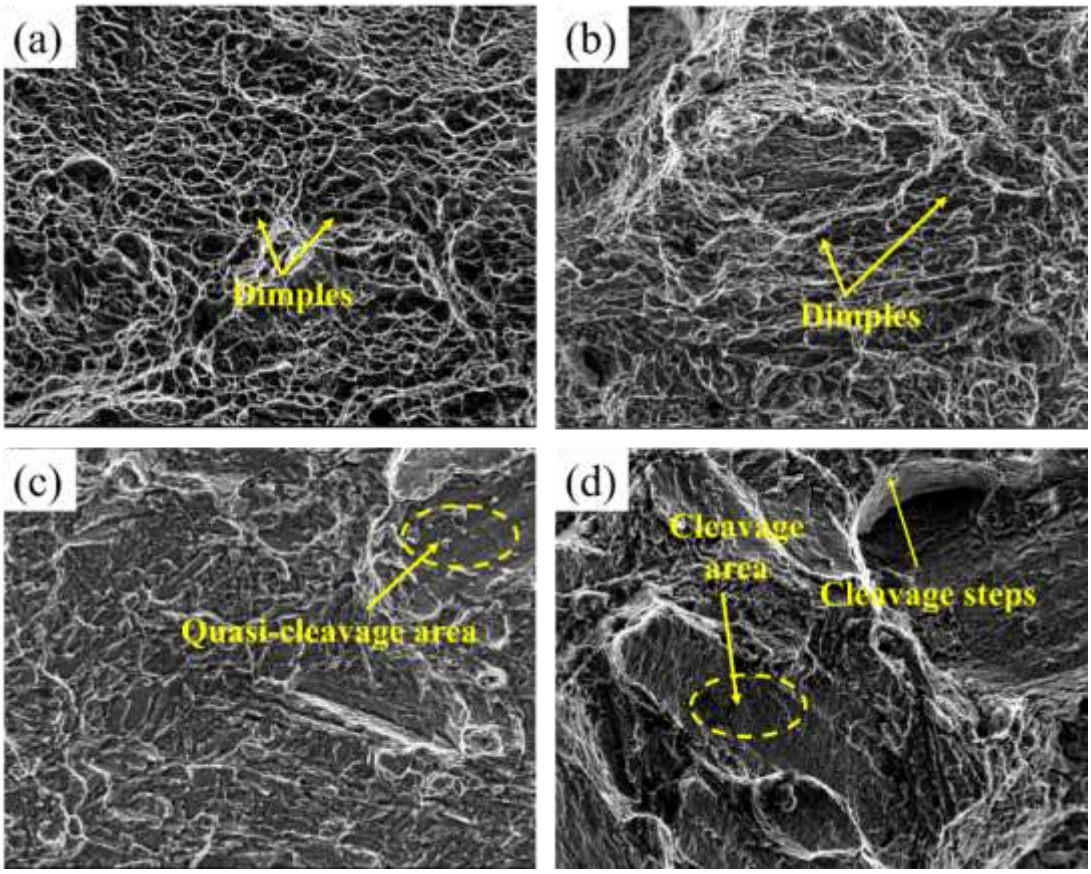

Figure 12. Evolution of the micro-fracture morphology of Ti6Al4V-$x$$Y_2O_3$: (a) Ti6Al4V, (b) Ti6Al4V-0.1 wt.%Y_2O_3, (c) Ti6Al4V-0.2 wt.%Y_2O_3, and (d) Ti6Al4V-0.3 wt.% Y_2O_3.

4. Discussion

4.1. Decomposition Behavior and Morphological Evolution of Y_2O_3 in the L-PBF Melt Pool

The morphological evolution of Y_2O_3 during the Ti6Al4V alloy fabrication process via L-PBF involves a complex interplay of high temperatures, rapid cooling, and dynamic reactions, as shown in Figure 13. The thermodynamic environment of this process is highly distinctive in that while the local temperature of the melt pool can reach a temperature of approximately 3000 °C, the melt lifetime is extremely brief—in the order of milliseconds—and is accompanied by cooling rates as high as 10^6–10^8 $K{\cdot}s^{-1}$. Under such non-equilibrium solidification conditions, Y_2O_3 (melting point = 2410 °C) evolves via two competing pathways.

On the one hand, the exceptionally high melt-pool temperature can induce the partial decomposition of Y_2O_3, producing elemental yttrium and oxygen atoms [39,40]. These highly reactive Y atoms are distributed throughout the Ti6Al4V melt. However, owing to the strong affinity between Y and O, they tend to recombine within the short melt lifetime, leading to the in-situ formation of Y_2O_3 nanoparticles.

On the other hand, and more importantly, the extremely rapid cooling rate significantly inhibits the complete decomposition and subsequent re-reaction of Y_2O_3 particles. The dominant evolution mechanism involves the mechanical fragmentation and refinement of Y_2O_3 particles under laser

 doi:10.20944/preprints202601.2384.v1

impact and intense Marangoni convection within the melt pool. The refined particles are ultimately dispersed throughout the Ti6Al4V matrix.

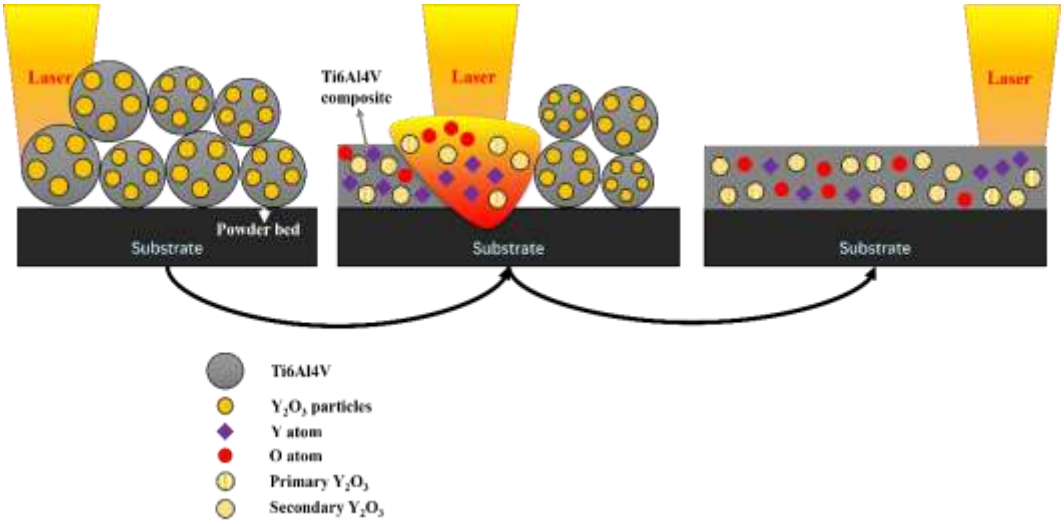

Figure 13. Decomposition behavior and morphological evolution of Y_2O_3 in the L-PBF melt pool.

4.2. Key Mechanism of Y_2O_3 in Grain Refinement

In the L-PBF processing of the Ti6Al4V alloy, the introduction of an appropriate amount of Y_2O_3 results in the precipitation and aggregation of nano-sized Y_2O_3 particles along grain boundaries. These particles serve as heterogeneous nucleation sites and facilitate grain refinement by pinning grain boundary migration. As the Y_2O_3 content increases, the grain refinement effect becomes more significant. Thus, the extent of grain refinement in Ti6Al4V alloys is strongly correlated with the nucleation rate (N) of Y_2O_3. According to the nucleation rate formula:

$$N = K_v \exp\left(-\frac{\Delta G_k}{kT}\right) \exp\left(-\frac{\Delta G_A}{kT}\right), \quad (1)$$

Where N denotes the nucleation rate, K_v is the proportionality coefficient, ΔG_k is the critical nucleation energy barrier, ΔG_A is the activation energy required for atoms to cross the solid–liquid interface, k is the Boltzmann constant, and T is the absolute temperature. The nucleation rate is strongly influenced by the critical nucleation energy barrier, which in turn is closely related to the interfacial energy (σ). The key finding of this study is that the incorporation of Y_2O_3 effectively lowers the nucleation interfacial energy. Rare earth oxides such as Y_2O_3 demonstrate favorable lattice matching with molten titanium. For example, the lattice mismatch between the (222) plane of Y_2O_3 and the (0001) plane of α-Ti is relatively small and markedly decreases the energy barrier for heterogeneous nucleation. Consequently, the reduction in interfacial energy directly initiates a significant drop in the critical nucleation barrier, thus promoting an exponential increase in the nucleation rate over a wide range of undercooling temperatures. This indicates that during L-PBF processing, the number of nucleation sites per unit volume increases substantially within the melt pool, establishing a fundamental prerequisite for grain refinement.

XRD analysis revealed that with increasing Y_2O_3 content, the diffraction peaks shift systematically toward higher angles (i.e., a rightward shift). Although measurement uncertainties may contribute to this shift, the consistent direction and regular progression of the angular change strongly suggests that Y_2O_3 incorporation induces lattice distortion in the material. To quantitatively assess this effect, calculations based on Bragg's law (Equation 2) and the α-phase interplanar spacing formula (Equation 3) were performed according to the methodologies reported in [42,43].

$$2d(hkl)\sin\theta = \lambda, \quad (2)$$

$$d(hkl) = \frac{a}{\sqrt{h^2+k^2+l^2}}, \quad (3)$$

 doi:10.20944/preprints202601.2384.v1

where *d(hkl)* denotes the interplanar spacing, θ is the diffraction angle, and λ is the wavelength of the X-ray (a constant). The rightward shift of the diffraction peaks of the α and β phases indicates an increase in the θ angle, leading to a decrease in interplanar spacing. According to Equation (3), a reduction in interplanar spacing suggests a decrease in the lattice constant *a*. This change reflects lattice contraction and distortion. The contraction of the lattice constant is a direct manifestation of lattice distortion, a further indication of structural changes in the material [44].

At the microscopic scale, lattice distortion increases the density of grain boundaries within the crystal and promotes the formation of substructures with diverse orientations. This effect manifests macroscopically as grain refinement. These findings are consistent with the microstructural evolution observed via EBSD in the preceding analysis, further confirming the role of Y_2O_3 addition in refining the crystal structure of the material.

The Y_2O_3-induced growth-restriction effect resulting from solute regulation may be a key reason for grain refinement. During solidification, solute enrichment or depletion at the solid–liquid interface front leads to constitutional supercooling. Within the constitutionally supercooled region, new nuclei are continuously forming, thereby increasing the nucleation rate. Solute accumulation effectively impedes the growth of existing nuclei, ultimately leading to grain refinement. To effectively utilize this effect, the solute must possess a high growth restriction factor (Q)—which can be defined as the rate of development of the constitutionally supercooled zone during solidification and calculated as follows:

$$Q = mC_0(k-1), \quad (4)$$

where Q is the rate of compositional undercooling induced by solute enrichment or depletion (K), m is the slope of the liquidus line in the binary phase diagram (K/(wt.%)). C_0 is the solute element concentration (wt.%), and k is the equilibrium distribution coefficient of the solute element. A higher rate of compositional undercooling produces a faster compositional undercooling formation rate and more significant grain refinement effect [45].

4.3. Strengthening Effect of Y_2O_3 on the Mechanical Properties of Ti6Al4V

The introduction of nanoscale Y_2O_3 particles in the T6Al4V alloy primarily enhances the mechanical properties of the material through the Orowan strengthening mechanism. This mechanism operates by using nanoscale Y_2O_3 as second-phase particles that hinder dislocation motion, thereby increasing material strength. The increment in Orowan strengthening can be expressed as follows [46]:

$$\Delta\sigma_{Oro} = \frac{0.13\, G_m\, m\, b}{\lambda} \ln\left(\frac{d}{2b}\right) \quad (5)$$

where G_m is the shear modulus of the matrix; b is the Burgers vector; d is the size of the Y_2O_3 particles within the grain; and λ denotes the particle spacing, which can be calculated as follows:

$$\lambda = d\left[\left(\frac{1}{2V}\right)^{1/3} - 1\right], \quad (6)$$

where V denotes the volume fraction of the precipitated phase within the grains. However, owing to the relatively low Y_2O_3 content within the actual grains and large inter-particle spacing, the contribution of the Orowan mechanism to the strength increment is small (approximately 0.68 MPa) and can be considered negligible in terms of overall strengthening.

The introduction of nanoscale Y_2O_3 particles also leads to the grain refinement of the Ti6Al4V matrix. This is attributed to the high melting point and thermal stability of Y_2O_3, which acts as a heterogeneous nucleation site, thus enhancing the nucleation rate. Furthermore, owing to the pinning effect, the nanoscale Y_2O_3 particles at the grain boundaries effectively restrict further grain growth. The strengthening effect resulting from grain refinement can be expressed by the Hall–Petch relationship [47] as follows:

$$\Delta\sigma_{HP} = k \cdot d^{-1/2}, \quad (7)$$

where k is a constant (247 MPa·(μm)$^{1/2}$ [48]) and d is the average grain size of the T6Al4V-xY_2O_3 alloys. In addition, Y_2O_3 particles can restrict dislocation motion through the pinning effect, thereby increasing dislocation density. This not only aids in grain refinement but may also further enhance

 doi:10.20944/preprints202601.2384.v1

strength by increasing the dislocation interactions. The empirical formula for dislocation density strengthening is expressed as follows:

$$\sigma_\rho = \sigma_0 + A \cdot \rho^{1/2}, \quad (8)$$

where σ_y is the yield strength of the material; σ_0 is the initial strength of the material (without dislocation effects); A is a constant related to the properties of the material; and ρ is the dislocation density (typically expressed in m^{-2}), with $\rho^{1/2}$ representing the square root of the dislocation density.

Because the various strengthening mechanisms do not act independently but rather synergistically, the increment in yield strength can be calculated by summing the squares of the contributions of each strengthening mechanism and then calculating the square root, as shown in the following formula:

$$\sigma_y = \sigma_{y0} + \Delta\sigma, \quad (9)$$

$$\Delta\sigma = \sqrt{(\Delta\sigma_{Oro})^2 + (\Delta\sigma_{HP})^2 + (\Delta\sigma_\rho)^2}, \quad (10)$$

where σ_y and σ_{y0} denote the yield strengths of the T6Al4V-$x$$Y_2O_3$ composite material and T6Al4V, respectively, and $\Delta\sigma$ denotes the total strength increment of the composite material in relation to T6Al4V. The final yield strength increment of approximately 70 MPa is in good agreement with the experimental results.

5. Conclusions

This study systematically explores the microstructure evolution and mechanical properties of Ti6Al4V-$x$$Y_2O_3$ composites fabricated via L-PBF technology. The results demonstrate that the introduction of Y_2O_3 particles during the L-PBF process results in the formation of nanoscale Y_2O_3 and elemental Y. The following conclusions regarding the mechanism of microstructure regulation and strengthening by Y_2O_3 particles in Ti6Al4V-$x$$Y_2O_3$ composites were drawn:

1. With increasing Y_2O_3 content, the microstructure of the Ti6Al4V alloy processed via L-PBF exhibited significant improvement. The average size of the β-phase grains was refined from 114.3 to 61.6 μm, and the average size of the α-phase grains decreased from 8.3 to 7.6 μm. TEM results showed that in the modified alloy with 0.2 wt.%Y_2O_3, Y_2O_3 and elemental Y nanoparticles (20–80 nm) were distributed between the α-Ti matrix and phase boundaries.
2. When the Y_2O_3 content was 0.2 wt.%, the tensile strength increased from 1056 to 1106 MPa, and the yield strength increased from 1001 to 1074 MPa; however, the elongation decreased from 15.4% to 10.0%. This indicates that although the rare earth oxide Y_2O_3 strengthens the mechanical properties of the Ti6Al4V alloy, it has a negative effect on ductility.
3. The refinement of the microstructure was mainly driven by the heterogeneous nucleation of Y_2O_3 and elemental Y nanoparticles, lattice distortion induced by them, and growth restriction effect mediated by solute elements.
4. The enhancement in mechanical properties was attributed to the combined effects of grain refinement strengthening (Hall–Petch mechanism), second-phase particle strengthening (Orowan mechanism), and dislocation density strengthening.

Funding: This work was supported by the Zhejiang Provincial Natural Science Foundation of China (No. LQN26E010002), "Leading Goose" R&D Program of Zhejiang [No. 2025C02206] and National Natural Science Foundation of China [No. 52304383].

Data Availability Statement: The original contributions presented in this study are included in the article. Further inquiries can be directed to the corresponding author.

Conflicts of Interest: The authors declare no conflicts of interest.

 doi:10.20944/preprints202601.2384.v1

References

1. Wang, Haobo; Tej N. Lamichhane; M. Parans Paranthaman. Review of additive manufacturing of permanent magnets for electrical machines: A prospective on wind turbine. *Materials Today Physics* **2022**, 24,100675.
2. Zhang, M.; Liu, C.; Deng, M.; Li, Y.; Li, J.; Wang, D. Graded Minimal Surface Structures with High Specific Strength for Broadband Sound Absorption Produced by Laser Powder Bed Fusion. *Coatings* **2023**, 13, 1950.
3. Song, J.; Chen, J.; Xiong, X.; Peng, X.; Chen, D.; Pan, F. Research advances of magnesium and magnesium alloys worldwide in 2021. *Journal of Magnesium and Alloys* **2022**, *10*(4), 863-898
4. Sheng, X.; Wang, A.; Wang, Z.; Liu, H.; Wang, J.; Li, C. Advanced surface modification for 3D-printed titanium alloy implant interface functionalization. *Frontiers in bioengineering and biotechnology*, **2022**, *10*, 850110.
5. Ghisheer, M.M.M.; Esen, I.; Ahlatci, H.; Akın, B. Investigation of Microstructure, Mechanics, and Corrosion Properties of Ti6Al4V Alloy in Different Solutions. *Coatings* **2024**, 14, 277.
6. Zhou, L.; Chen, J.; Li, C.; He, J.; Li, W.; Yuan, T.; Li, R. Microstructure tailoring to enhance strength and ductility in pure tantalum processed by selective laser melting. *Materials Science and Engineering: A*, **2020**, *785*, 139352.
7. Li, R.; Yue, H.; Luo, S.; Zhang, F.; Sun, B. Microstructure and mechanical properties of in situ synthesized (TiB+ TiC)-reinforced Ti6Al4V composites produced by directed energy deposition of Ti and B4C powders. *Materials Science and Engineering: A*, **2023**, *864*, 144466.
8. Wang, L.; Song, Z.; Zhang, X.; Park, J. S.; Almer, J.; Zhu, G.; Li, Y. Developing ductile and isotropic Ti alloy with tailored composition for laser powder bed fusion. *Additive Manufacturing*, **2022**, *52*, 102656.
9. Zhang, R.; Zhao, S.; Ophus, C.; Deng, Y.; Vachhani, S. J.; Ozdol, B.; Minor, A. M. Direct imaging of short-range order and its impact on deformation in Ti-6Al. *Science advances*, **2019**, *5*(12), 2799.
10. Meng, X.; Min, J.; Sun, Z.; Zhang, W.; Chang, H.; Han, Y. Columnar to equiaxed grain transition of laser deposited Ti6Al4V using nano-sized B4C particles. *Composites Part B: Engineering*, **2021**, *212*, 108667.
11. DebRoy, T.; Mukherjee, T.; Wei, H. L.; Elmer, J. W.; Milewski, J. O. Metallurgy, mechanistic models and machine learning in metal printing. *Nature Reviews Materials*, **2021**, *6*(1), 48-68.
12. Liu, S.; Shin, Y. C. Additive manufacturing of Ti6Al4V alloy: A review. *Materials & Design*, **2019**, *164*, 107552.
13. Lu, S.; Li, Y.; Zhen, S.; Yu, D.; Zhang, L.; Chen, R.; Li, S. Influence of process parameters on the microstructures, residual stresses and mechanical properties of TA15 titanium alloy fabricated by L-PBF. *Materials Science and Engineering: A*, **2025**, *927*, 147990.
14. Tan, S. Y.; Yan, Z. L.; Zeng, W. H.; Zhao, Y.; Wang, C. Y.; Yang, Y. Microstructural Variation and Mechanical Properties in PBF-LB/M Ti-6Al-4V: The Role of Large Build Height. *Materials Science and Engineering: A*, **2025**, 149042.
15. Wang, X.; Zhang, L. J.; Ning, J.; Li, S.; Na, S. J. Effect of addition of micron-sized lanthanum oxide particles on morphologies, microstructures and properties of the wire laser additively manufactured Ti–6Al–4V alloy. *Materials Science and Engineering: A*, **2021**, *803*, 140475.
16. Zhang, T.; Xiao, H.; Zhang, Z.; Yao, B.; Yang, F. Effect of Y2O3 addition on microstructural characteristics and microhardness of laser-cladded Ti-6Al-4V alloy coating. *Journal of Materials Engineering and Performance*, **2020**, *29*(12), 8221-8235.
17. Kennedy, J. R.; Davis, A. E.; Caballero, A. E.; Byres, N.; Williams; S.; Pickering, E. J.; Prangnell, P. B. β Grain refinement by yttrium addition in Ti-6Al-4V Wire-Arc Additive Manufacturing. *Journal of Alloys and Compounds*, **2022**, *895*, 162735.
18. Wang, X.; Zhang, L. J.; Ning, J.; Li, S.; Zhang, L. L.; Long, J. Hierarchical grain refinement during the laser additive manufacturing of Ti-6Al-4V alloys by the addition of micron-sized refractory particles. *Additive Manufacturing*, **2021**, *45*, 102045.
19. Li, S.; Wang, X.; Wei, Z.; Han, Y.; Shi, H.; Le, J.; Lu, W. Simultaneously improving the strength and ductility of the as-sintered (TiB+ La2O3)/Ti composites by in-situ planting ultra-fine networks into the composite powder. *Scripta Materialia*, **2022**, *218*, 114835.

20. Liu, Y.; Song, Z.; Guo, Y.; Zhu, G.; Fan, Y.; Wang, H.; Wang, L. Simultaneously enhancing strength and ductility of LPBF Ti alloy via trace Y2O3 nanoparticle addition. *Journal of Materials Science & Technology*, **2024**, *191*, 146-156.
21. Zhou, L.; Yang, X.; Chen, J.; Ren, Y.; Niu, Y.; Qiu, W.; Li, C. Muti-mechanism of the improving wear performance for titanium alloy via laser powder bed fusion. *Journal of Materials Research and Technology*, **2024**, *30*, 3186-3199.
22. Cui, W. F.; Liu, C. M.; Zhou, L.; Luo, G. Z. Characteristics of microstructures and second-phase particles in Y-bearing Ti-1100 alloy. *Materials Science and Engineering: A*, **2002**, *323*(1-2), 192-197.
23. Hotta, S.; Yamada, K.; Murakami, T.; Narushima, T.; Iguchi, Y.; Ouchi, C. β grain refinement due to small amounts of yttrium addition in α+ β type titanium alloy, SP-700. *ISIJ international*, **2006**, *46*(1), 129-137.
24. Poorganji, B.; Kazahari, A.; Narushima, T.; Ouchi, C.; Furuhara, T. Effect of yttrium addition on grain growth of α, β and α+ β titanium alloys. 15th International Conference on the Strength of Materials. Germany, 16–21 August 2009.
25. Zhu, X.; Jiang, Z.; Liu, Z.; Wang, N.; Xu, Y. Trace Y for as-cast Ti6Al4V to simultaneous enhance strength-ductility. *Journal of Alloys and Compounds*, **2023**, *948*, 169757.
26. Beladi, H.; Chao, Q.; & Rohrer, G. S. Variant selection and intervariant crystallographic planes distribution in martensite in a Ti–6Al–4V alloy. *Acta Materialia*, **2014**, *80*, 478-489.
27. Wang, X.; Zhang, L. J.; Ning, J.; Li, S.; Zhang, L. L.; Long, J. Hierarchical grain refinement during the laser additive manufacturing of Ti-6Al-4V alloys by the addition of micron-sized refractory particles. *Additive Manufacturing*, **2021**, *45*, 102045.
28. Simonelli, M.; Tse, Y. Y.; Tuck, C. On the texture formation of selective laser melted Ti-6Al-4V. *Metallurgical and Materials Transactions A*, **2014**, *45*(6), 2863-2872.
29. Yao, Z.; Yang, T.; Yang, M.; Jia, X.; Wang, C.; Yu, J.; Liu, X. Martensite colony engineering: A novel solution to realize the high ductility in full martensitic 3D-printed Ti alloys. *Materials & Design*, **2022**, *215*, 110445.
30. Zhang, X.; Xu, H.; Li, Z.; Dong, A.; Du, D.; Lei, L.; Sun, B. Effect of the scanning strategy on microstructure and mechanical anisotropy of Hastelloy X superalloy produced by Laser Powder Bed Fusion. *Materials Characterization*, **2021**, *173*, 110951.
31. Jiang, J.; Ren, Z.; Ma, Z.; Zhang, T.; Zhang, P.; Zhang, D. Z.; Mao, Z. Mechanical properties and microstructural evolution of TA15 Ti alloy processed by selective laser melting before and after annealing. *Materials Science and Engineering: A*, **2020**, *772*, 138742.
32. Gil, F. J.; Planell, J. A. Behaviour of normal grain growth kinetics in single phase titanium and titanium alloys. *Materials Science and Engineering: A*, **2000**, *283*(1-2), 17-24.
33. Yang, J.J. Microstructure evolution and control of Ti6Al4V alloy fabricated by selective laser melting. Master's Thesis, Huazhong University of Science and Technology, Wuhan, 2017.
34. Massalski, T.B.; Okamoto, H.; Subramanian, P.R.; Kacprzak, L. *Binary Alloy Phase Diagrams*; ASM International: Materials Park, USA, 1990; pp. 852.
35. Wang, X.; Zhang, L.J.; Ning, J.; Li, S.; Zhang, L.L.; Long, J. Hierarchical grain refinement during the laser additive manufacturing of Ti-6Al-4V alloys by the addition of micron-sized refractory particles. *Additive Manufacturing*, **2021**, 45, 102045.
36. Hayes, B. J.; Martin, B. W.; Welk, B.; Kuhr, S. J.; Ales, T. K.; Brice, D. A.; Collins, P. C. Predicting tensile properties of Ti-6Al-4V produced via directed energy deposition. *Acta Materialia*, **2017**,*133*, 120-133.
37. Yang, J.; Xiao, S.; Yuyong, C.; Xu, L.; Wang, X.; Zhang, D.; Li, M. Effects of nano-Y_2O_3 addition on the microstructure evolution and tensile properties of a near-α titanium alloy. *Materials Science and Engineering: A*, **2019**, 761, 137977.
38. Han, W.; Min, J.; Dai, G.; Guo, Y.; Chang, L.; Wang, Y.; Chang, H. Effect of Y_2O_3 addition on microstructure and properties of Ti6Al4V by laser melting deposition. *Materials Science and Engineering: A*, **2023**, 886, 145694.
39. Quazi, M.M.; Fazal, M.A.; Haseeb, A.S.M.A.; Yusof, F.; Masjuki, H.H.; Arslan, A. Effect of rare earth elements and their oxides on tribo-mechanical performance of laser claddings: A review. *Journal of Rare Earths*, **2016**, 34(6), 549-564.

 doi:10.20944/preprints202601.2384.v1

40. Weng, F.; Yu, H.; Chen, C.; Liu, J.; Zhao, L. Microstructures and properties of TiN reinforced Co-based composite coatings modified with Y_2O_3 by laser cladding on Ti–6Al–4V alloy. *Journal of Alloys and Compounds*, **2015**, 650, 178-184.
41. Wang, L.; Yang, L.; Huang, Y.; Yuan, Y.; Jia, C. Effects of Y_2O_3 addition on the microstructure and wear-resistant performance of TiN/TiB-reinforced Ti-based laser-clad coatings on Ti-6Al-4V alloys. *Materials Today Communications*, **2021**, 29, 102752.
42. Fan, Q. A new method of calculating interplanar spacing: the position-factor method. *Applied Crystallography*, **2012**, 45(6), 1303-1308.
43. Pope, C.G. X-ray diffraction and the Bragg equation. *Journal of Chemical Education*, **1997**, 74(1), 129.
44. Skvortsova, S.; Grushin, I.; Umarova, O.; Speranskiy, K. Effect of Rare-earth Element Addition on Structure of Heat-resistant Ti–6.5 Al–4Zr–2.5 Sn–2.4 V–1Nb–0.5 Mo–0.2 Si Titanium Alloy. In Proceedings of the 2017 International Conference on Mechanical, Material and Aerospace Engineering, Moscow, Russia, 2017.
45. Okamoto, H.; Schlesinger, M.E.; Mueller, E.M. *Alloy Phase Diagrams*; ASM International: Materials Park, USA, 2016.
46. Ramakrishnan, N.J.A.M. An analytical study on strengthening of particulate reinforced metal matrix composites. *Acta Materialia*, **1996**, 44(1), 69-77.
47. Chen, Y.; Yang, C.; Fan, C.; Zhuo, Y.; Lin, S.; Chen, C. Grain refinement of additive manufactured Ti-6.5 Al-3.5 Mo-1.5 Zr-0.3 Si titanium alloy by the addition of La_2O_3. *Materials Letters*, **2020**, 275, 128170.
48. Guo, X.; Wang, L.; Wang, M.; Qin, J.; Zhang, D.; Lu, W. Effects of degree of deformation on the microstructure, mechanical properties and texture of hybrid-reinforced titanium matrix composites. *Acta Materialia*, **2012**, 60(6-7), 2656-2667.